Mechanical power modulation of iPAM soft actuators through exhaust flow regulation for scalable mobile pneumatic robots

Trifko Basic, and Matthew A. Robertson, *Member, IEEE*

***Abstract*—A new strategy is proposed for modulating the mechanical power output of an inverse pneumatic actuator muscle (iPAM), by designing a valve mechanism to regulate the flow of internal pressurized air exhausted to atmosphere during the iPAM's power stroke in contraction from an inflated initial state. Since the regulation is performed on the unpressurized exhaust line which does not need to work against relatively high supply pressure, the design of the valve is simplified compared to other off-the-shelf or commercially available regulator solutions, allowing it to be lightweight, easy to fabricate, and low-cost to facilitate its use in customized, lightweight pneumatically powered robot applications. A custom proportional flow regulation valve known as a servo-actuated obstruction of fluid flow device (SOFD) is presented which changes the effective cross-sectional area of a fluid flow path connected in-line with the iPAM exhaust. The resulting change in exhaust flow rate from the actuator allows for variable power applied by the actuator to be specified for the same initial energy stored in the iPAM by a fixed pressure. To control the system via the SOFD, a model is developed which relates a desired power or energy output to an effective orifice area that can be set by the SOFD. The model is validated by comparing measured launch heights of a mass to predicted heights. Experimental results show the model's effectiveness, demonstrating the practical utility of the proposed strategy for controlled power modulation in elastic energy storage-based contractile SPAs similar to iPAMs.**

***Index Terms*—Soft pneumatic actuators, valve design, regulator design, 3D printed robots, legged robots**

I. Introduction

Legged locomotion offers the ability to effectively negotiate unstructured and challenging environments. In nature, legs are exploited for their inherent adaptability to different terrains [1], [2], [3] but also for their versatility in how they can be employed for locomotion, which include walking, running. or hopping and jumping [4], This variety enables animals to traverse a wide range of uneven or cluttered ground conditions often encountered in the real world. Due to the diversity and utility of legged locomotion observed in the animal kingdom, significant research has been dedicated to developing bio-inspired robots that emulate the different capabilities and mechanisms observed in nature [5], [6], [7], [8], [9] to leverage the benefit of legs in machines.

Legged robots have been demonstrated at various sizes and power scales with particular recent interest in achieving dynamic, agile, and robust performance. Sophisticated walking and running robots have been developed which are capable of two-legged (bipedal) [10], [11], [12] and four-legged (quadrupedal) [13], [14], [15], [16] locomotion. The motion of these relatively large-scale robots is driven either by hydraulic or electric actuators in order to achieve the high-power required to perform dynamic maneuvers, such as jumping. Although these robots leverage some passive compliance, often through the use of springs, in complement to powered actuation where possible to achieve certain performance benefits including robustness and efficiency [17], it is impractical to offload a significant amount of power production from actuation to these compliant components due to the amount of energy storage required to perform certain maneuvers such as high hopping or jumping [18] with high-mass systems. For this reason, other types of larger (macro) scale jumping robots more commonly employ direct drive actuation to achieve jumps using electric motors or pneumatic actuators [19], [20]. At smaller scales (meso scale and below) however, robots with lower mass can leverage the benefits of springs to store and release mechanical energy to perform high jumps (heights above their resting body center of mass) and dynamic motions without the use of directly powered actuators [21], [22], [23], [24], [25].

Soft pneumatic actuators (SPAs) have been used as a method for driving robots which simultaneously provide force generation and natural compliance but can also be exploited for their energy storage capabilities to achieve high-power actuation. SPAs are generally described as hollow elastic structures which perform work that can be used for actuation as a result of inflation from a pneumatic pressure source. Typically fabricated from compliant elastomer materials, SPAs, which include pneumatic artificial muscles (PAMs) [26] or McKibben actuators [27], have been shown to demonstrate high power-to-weight ratios, which offer benefits to a diverse range of emerging robotic applications [28], [29]. Despite their exceptionally low weight compared to alternative actuation sources predominantly used in robotics however, SPAs have most commonly been employed in relatively low-speed, low-power tasks as a result of the significant energy that is effectively lost in the process of actuation due to the inflation of their elastic structures. In addition, the power output of SPAs is often limited by the pressure source which they are driven by. Although high-power action such as jumping is possible to achieve using SPAs and has been demonstrated using McKibben actuators [30], it requires high-pressure pneumatic source to compensate for the energy demand of inflation, requiring high pressure or

T. Basic and M. Robertson are with the Novel Engineering and Robotic Devices (N.E.R.D.) research laboratory in the Mechanical and Materials Engineering (M.M.E.) Department and Ingenuity Labs Research Institute, Queen's University, Kingston, Canada.

flow rate pumps and correspondingly rated hardware that is not suitable for lightweight, mobile robot platforms.

Due to the limited selection or out-of-scale physical attributes of off-the-shelf (OTS) hardware components typically used for power and control of pneumatic systems utilized in soft robotics, another distinguishing feature of these systems – their customizability – is easily undercut by the overhead design cost of integrating non-customizable components. In general, OTS pneumatic system components for controlling soft robots are neither optimized for their scale, in terms of mass or size, nor for their fabrication and integration, which utilize primarily compliant or low-cost materials. Moreover, soft robots increasingly leverage 3D printing or other unique fabrication processes in the aim to achieve fully integrated fluid-powered machines. These system attributes have motivated other researchers to therefore design customizable control hardware components, including valves [31], [32], [33], [34], pumps [35], [36], and fluidic-logic elements [37], [38], [39] which are better suited for the materials, techniques, and final applications the soft robotic systems are designed for. Regardless of the intended end-use or level of optimization, however, the design of fluidic switching or regulation components in any domain (rigid or soft) must contend with the physical constraints and challenges presented by pressurized fluid power modulation, including sealing, fluid-force effects, and control characteristics, which may limit their use in certain applications.

As the type and function of power and control hardware is closely coupled to the type and function of the actuator being controlled, the challenge of developing more customizable and scalable hardware can be simplified in part by appropriate actuator selection. Following an alternate approach to the design and function of most SPAs, the inverse PAM (iPAM) is a unique example of SPA which has previously demonstrated the capacity to facilitate high-power actuation [40] while also introducing new opportunities for control. While the force resulting from elastic energy stored in the material of most SPAs typically opposes the direction of their powered actuation from pressure driven inflation, iPAMs employ the release of stored energy itself for actuation. Comprising a hollow elastic core wrapped with inextensible fibers, the iPAM extends linearly as it is inflated with pressurized air prior to actuation. Once pre-strained, or primed, in this way, the iPAM can be activated by releasing its internally pressurized air. As pressurized air is released, the actuator contracts in tension through its power stroke, driven by the energy returned by its stretched elastic core, and this nominally rapid contraction can be used to perform high-power mechanical work.

The difference in function of iPAMs motivates a new approach to their control and implementation in a pneumatically powered robotic system. Generally, most SPAs are pressure controlled, either through a continuously variable pressure regulator or through pulse-width modulation of a discrete solenoid valve emulating pressure control via a form of discretized flow control. Either method allows the force or speed of actuator inflation to be varied proportionally to its controlled internal pressure, directly enabling modulation of the actuator's power output. In both cases, however, the modulation of air supplied to the SPA occurs on the high side of the pneumatic control circuit, in direct connection with the pressurized air source. In this configuration, the control components themselves must be designed to withstand constant exposure to the operating supply pressure, and simultaneously perform the function of regulation or flow switching. From a hardware design perspective, this requires precision tolerances and material selections to accommodate the sealing of moving internal parts, such as valve shuttles or poppets. Under high-pressure conditions, it is likewise important (if not one of the main challenges of valve design) to carefully consider the effect of the force from pressurized air on the internal mechanisms and actuation technology which are designated for actually switching the air flow. Due to this effect, certain simple mechanisms or methods for switching fluid flow, such as poppet, butterfly, or gate valves, do not work well with high-pressure fluid and low-force actuators, as the process of redirecting fluid (required for changing either pressure or flow) also involves working against the force of the fluid itself on the valve mechanics.

In this work, we present a novel hardware-based technique for controlling the power output of iPAMs with a custom-fabricated flow control mechanism, compatible with system design and fabrication techniques commonly employed in soft robotics. In contrast to the working principle of most pressure or flow control devices, OTS or custom built, the hobby servo-powered flow control regulator, deemed the servo obstruction of fluid flow device (SOFD) employs a gate valve mechanism to vary the flow of fluid on the low-pressure side of the pneumatic control circuit, serving to regulate the actuator exhaust line rather than its high-pressure supply line. This unique configuration relaxes some of the most critical design requirements for valve or regulator design, enabling a low-cost, readily manufacturable SOFD to be constructed using low dimensional tolerance 3D printed parts and relatively low-force switching actuator (micro servo). In order to modulate the power output from this proposed regulator and pneumatic circuit control topology, we perform initial fluid-dynamics characterization studies to generate a model relating the SOFD actuator position input to the resulting iPAM actuation power output. Our model is validated through comparison with experimental results of an iPAM-driven vertical catapult mechanism, which serves not only as a predictable benchtop demonstration but also as a simplified representation of a jumping robot leg which could be refined and integrated in future work to a full legged mobile robot platform.

II. Design

A. *iPAM exhaust flow regulation valve design*

The proposed exhaust flow regulation valve, servo obstruction fluid flow device (SOFD), consists of inexpensive and 3D printed components using the Original Prusa i3 MK3S+. An off-the-shelf Miuzei SG90 9 g micro-servo motor is used to actuate the custom valve to regulate the flow and has a stall torque of 2.0 ± 0.20kg·cm (4.8V). A 3D printed pinon was adapted onto the servomotor's output gear to transfer the servomotor's torque to a 3D printed rack, achieving the transfer of rotational motion of the servomotor to linear motion of the rack. To regulate the flow a housing for the servomotor, pinion, and rack was designed to connect the exhaust air flow path with the rack, making it possible for the rack to obstruct the exhaust air flow. Overall, the valve works by sending the servomotor an angular position which is than translated by the pinion and rack to a linear position, therefore modifying the area of the exhaust air flow's path to atmosphere (Fig. 1). The reduced area of the exhaust flow path through the regulator thereby reduces the flow rate of the air, and hence the retraction speed and power of the iPAM contraction.

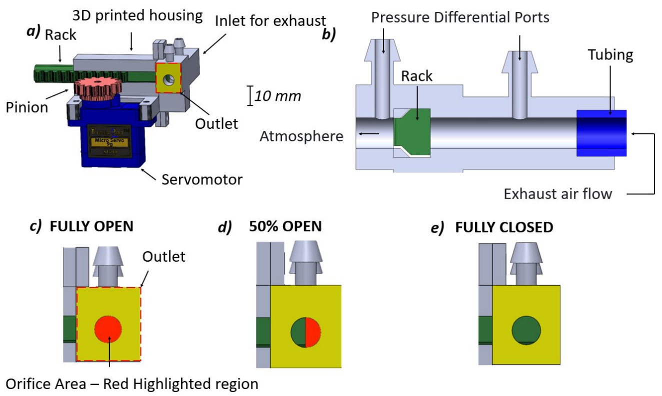

Fig. 1: Custom built exhaust air flow regulator - SOFD: ***a)*** 3D model of air flow regulator that includes a 3D printed housing, rack, pinion, and servomotor that make up the SOFD. ***b)*** Section view of the exhaust air flow incoming from the solenoid valve where the rack obstructs the exhaust air flow path to atmosphere. The two pressure ports are there to measure the pressure drop across the orifice from a pressure differential sensor. Subfigures ***c)***, ***d)***, and ***e)*** depicts front views of the outlet of the exhaust air flow path, for different example occluded orifice areas. As the linear position of the rack changes, the area of the outlet changes and the amount of exhaust flow obstruction is therefore varied.

Solely using 3D printed parts with no additional seals or further machining to improve on the parts is acceptable because the SOFD is implemented on the exhaust line. Traditional off-the-shelf flow regulators connected in-line with an active pressure source have major constrains to their designs. One constraint is that more forces need to be overcome when connected to an active pressure source requiring a stronger actuator, leading to more expensive and heavier flow regulators. Another constrain is the need for a fully sealed system to prevent air leaks from the pressure source and the fabrication procedure for sealed moving components is often complex requiring multiple materials and is not tailored towards a lightweight or inexpensive solution. Without these constraints, primarily due to being on the exhaust line, means that fully sealing the valve is not necessary and a lightweight micro-servomotor can be used to actuate the flow regulating mechanism. The Original Prusa i3 MK3S+ 3D printer has good tolerance, resolution and smoothness making the 3D printed components fit well together and despite leakages occurring in the valve, barbed fittings on the housing are ports for a pressure differential sensor that will be used in the methodology section to take air leakage into account when modeling the iPAM's power output.

B. Linear Constrained Housing for iPAM

The iPAM is custom made consisting of off-the-shelf natural latex rubber tube with a diameter of 12.77 mm, wall thickness of 1.59 mm, and cut to a length of 70 mm. The tube was wrapped with a 10-lb rated fishing line that is meant to constrain the tube's motion during inflation and contraction to strictly linear motion along the central axis of the tube. The fishing line was adhered only to the ends of the latex tube, leaving the possibility of the fishing line threads shifting during the tube's inflation or contraction. Wherever the thread would slip revealing the latex tube would result in the tube radially expanding, and thus no longer having the desired linear motion. To minimize this risk, Elastosil M 4601 was brushed over the latex tube and fishing line to create a skin layer that helps keep the fishing in place. Due to the natural latex tubing being pre-formed, along with the non-uniform wrapping of the fishing line, the longitudinal dimension of the iPAM is biased with a light curvature. To restrict the iPAM's motion from bending and buckling, a housing for the iPAM was designed consisting of a supply air cap with linear guide bearing tubes and an end cap with stainless steel guide rods (Fig. 2). The linear guide bearing tubes extend entirely through the supply air cap component to facilitate smooth linear motion and support of the guide rods throughout long near strokes near maximum actuator extension. Both caps were 3D printed using an Original Prusa i3 MK3S+ from PLA, resulting in an overall weight of the complete iPAM with its linear constrained housing to be 26 g.

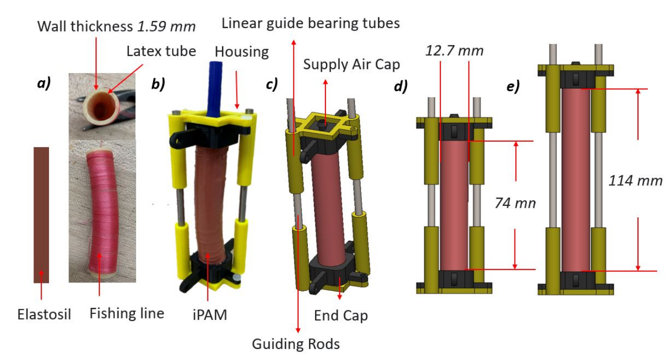

Fig. 2: Linear constrained iPAM: ***a)*** Top and front view of the latex rubber actuator core wrapped in fishing line. ***b)*** The iPAM assembled with its housing. ***c)*** 3D model of the iPAM and the two separate 3D printed components that make up the linear constrained housing for the iPAM. ***d)*** Illustrates the iPAM and its housing in its contracted state. ***e)*** Illustrates the extension of the iPAM when inflated to a certain supplied pressure.

During inflation the iPAM stores its elastic energy as the latex rubber is being stretched out by the supplied pressure and when the internal pressurized air of the iPAM is exhausted to atmosphere, the actuator contracts back to its original length, rapidly releasing its stored energy from inflation. Since actuation power is produced by the contraction of the iPAM, a device for regulating the exhaust air flow of the iPAM can be exploited as a method to modulate the iPAM's power output, which is fundamentally a function of actuator force and velocity. Regulating the flow of the exhaust air allows for power modulation because the exhaust flow rate affects the speed at which the iPAM contracts while the actuation force from elastically stored energy is only a function of iPAM displacement and therefore is independent of the change in flow rate.

Fig. 3, illustrates a simple control scheme for actuating the iPAM starting with opening a 3/2 solenoid valve allowing air at a fixed pressure to fill the actuator to maximum extension and stored energy in the tubing of the iPAM, priming the actuator. To set the contraction speed, and hence power output level of the iPAM, the SOFD can be adjusted to an appropriate position for a specified air flow. This can be done independent of the supply pressure side of the circuit and asynchronously, not requiring to be adjusted proportionally in a closed loop to achieve flow. Once the valve area is set, the solenoid valve switches states to close off the supply line and connects the iPAM to the exhaust line for the actuator's power stroke, exhausting the iPAM's internal pressurized air to atmosphere, releasing its energy and using it to actuate some mechanism.

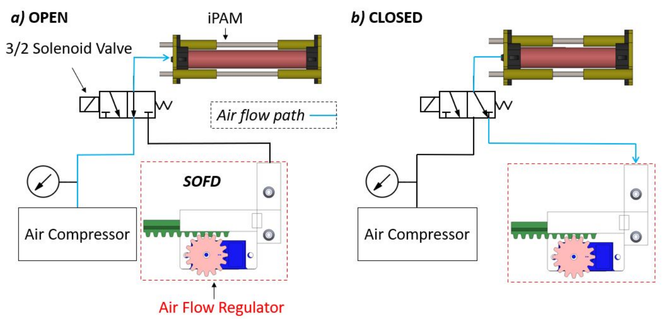

Fig. 3: Pneumatic Circuit for exhaust flow regulation: The pneumatic circuit consists of an air compressor, pressure gauge, 3/2 solenoid valve, an iPAM, and an air flow regulator on the exhaust line. The proposed SOFD is integrated into this pneumatic circuit as the air flow regulator. There are two states: ***a)*** when the pressure source is connected to the iPAM, inflating the iPAM and priming the actuator and ***b)*** when the iPAM is connected to the SOFD that is connected to atmosphere, exhausting the iPAM's internal pressurized air, causing a power stroke.

C. Exhaust flow regulation power-modulated vertical catapult

A simple mechanism was created with the Original Prusa i3 MK3S+ to 3D print a linkage and plate (Fig. 4). The linkage translates the iPAM's contracting power stroke into the plate's vertical acceleration. The supply air cap is fixed, and the end cap is free to slide in the horizontal axis, the distance between the supply air cap and end cap is the iPAM's length l. With the plate positioned above the supply air cap, the linkage restricts the plate to vertical displacement only. This distance from the supply air cap to the plate is the plate's height h. This mechanism is secured with 3D printed brackets into slotted T beams and linear bearings restricting the plate from tilting, ensuring that it remains level with the ground throughout its motion. The mechanism with its T slotted beam housing results in a launching mechanism that leverages the iPAM's power stroke by transferring its contraction motion through a linkage accelerating the plate vertically to launch a projectile placed on top of the plate. The purpose of this mechanism is to validate if the iPAM's power modulation can be transferred to a projectile's maximum launch height being modulated.

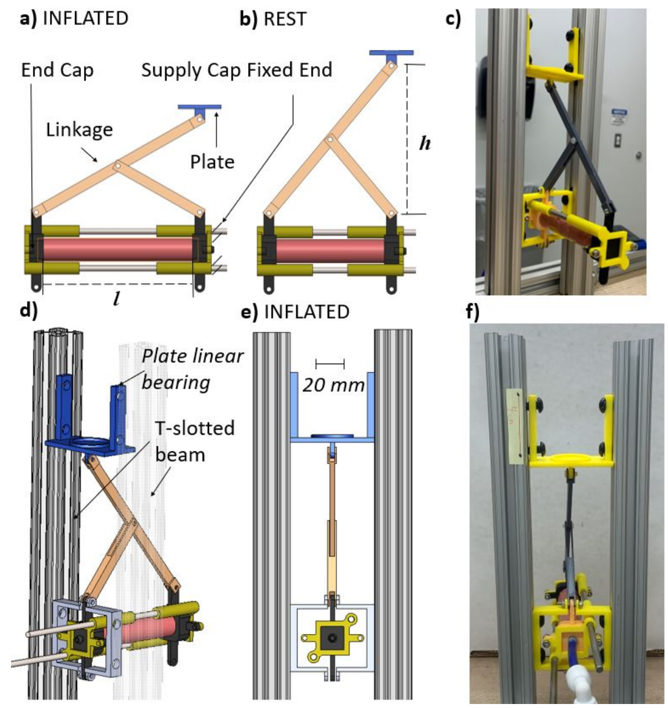

Fig. 4: iPAM actuated vertical launching mechanism: ***a)*** The iPAM is initially inflated with a fixed pressure and primed at its maximum extension. Since the supply air cap is fixed, only the end cap's horizontal position changes when the pressurized iPAM contracts on depressurization as air is released. The plate is at its minimum height in this case. ***b)*** In its rest state the iPAM is fully contracted, and its internal pressure is equal to atmosphere. The plate is at its maximum height in this case. ***c)*** Photo of the launcher mechanism integrated iPAM ***d)*** A 3D model of the complete vertical catapult mechanism with the T-slot beams that keep the plate position level with the ground. ***e)*** Front view of the catapult when the iPAM is inflated. ***f)*** Image of the assembled iPAM vertical catapult.

III. Methodology

To predictably control the power output of an iPAM using the SOFD as an exhaust flow regulator a procedure was developed to characterize the contraction velocity of the iPAM as a function of the exhaust orifice area. The iPAM's power stroke occurs when it exhausts its internal pressurized air, which releases the stored energy from the stretched latex tubing, causing it to contract back to its rest state. To achieve this goal, empirical tests were conducted, and a model was developed that takes an orifice area as input and outputs the iPAM's contraction displacement versus time curve. 3D printed orifice meters, each with a different fixed orifice area, were used to estimate the flow rate accurately since using the SOFD directly would make it difficult to calculate the flow rate due to imperfect sealing and air leaks which are inherent to its design. The orifice meters were related to the SOFD, and the model was used to achieve an output of the iPAM's contraction displacement versus time curve from an SOFD input. To validate this methodology, this output was applied to the vertical catapult mechanism, and the model was tested to see if it could accurately predict the projectile's maximum launch height. Fig. 5 illustrates the workflow diagram of the entire methodology, beginning with the characterization of the iPAM and ending with the approximate projectile maximum launch heights. The details of the workflow diagram will subsequently be described in the next sections.

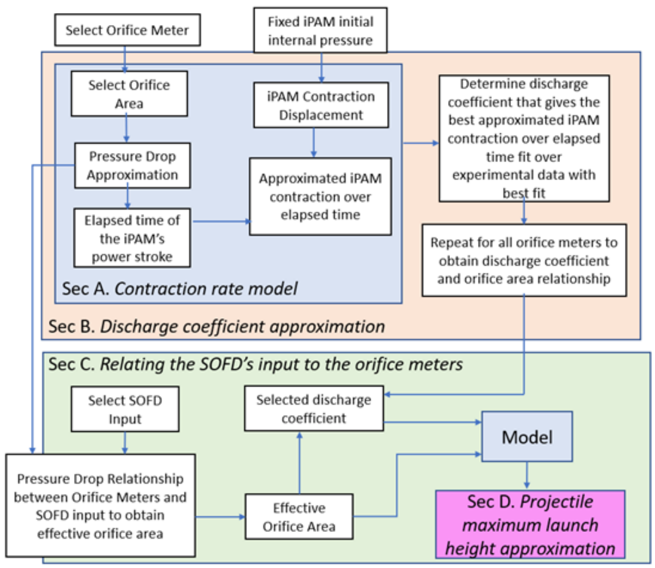

Fig. 5: Methodology Workflow diagram: A high-level outline of the approach taken to predict a projectile's maximum launch height as a function of the exhaust orifice area. Each coloured box represents one of the subsections of the "Methodology" section to make it easier to connect the text with its corresponding parts in the diagram.

A. Contraction rate model

The model's objective is to output two parameters: the displacement of the iPAM and the time it takes to complete its power stroke. These two parameters are independent of each other since the iPAM's displacement is only affected by the pressure supplied to it, while the time is affected by the flow rate of the exhaust air. As a result, different empirical tests are conducted to obtain each parameter.

1) Characterization of iPAM pressure versus displacement: Regulating the flow has no effect on the iPAM's displacement during its prime or power stroke. The prime stroke is when the iPAM is inflating, hence extending, and the power stroke is when the iPAM is contracting. The pressure applied to the iPAM is the driving force that stretches the tubing to inflate to a certain length. Observing the displacement of the iPAM as it is inflated at different pressures will also provide the iPAM's displacement during contraction because the iPAM undergoes a pressure change from exhausting its internal pressurized air to atmosphere. The only difference between extension and contraction displacement is the direction. A displacement versus supplied pressure test was performed starting at a supplied pressure of 0 kPa increasing the pressure and measuring the iPAM's displacement until 300 kPa was reached (Fig. 6). A quadratic function was fit to the experimental results that produces a function that takes in a pressure in kPa and outputs the iPAM's displacement in mm. The displacement of the iPAM is used to approximate its change in volume during the power stroke. It is assumed that the iPAM's volume can be approximated by the geometry of a perfect cylinder, and that any radial deformation can be ignored since the outside wall is restrained by the fishing line. As a result, only the length of the iPAM changes during the power stroke. This approximation of volume will be used to help approximate the time it takes for the iPAM to complete its power stroke.

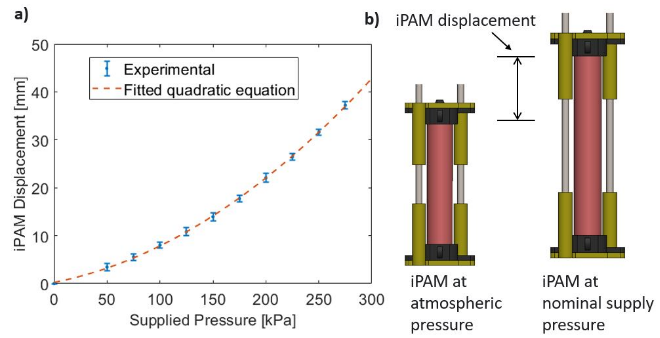

Fig. 6: iPAM pressure versus displacement: ***a)*** Plot illustrating the relationship between the pressure supplied to the iPAM versus the iPAM's displacement caused by the supplied pressure. ***b)*** An illustration of the measured iPAM displacement between the iPAM's unpressurized state and pressurized state.

2) Procedure for approximating the elapsed time of the iPAM's power stroke: The exhaust air's flow rate is approximated by using compressible fluid theory [41]. Air is treated to be compressible and turbulent resulting in the following equations for flow rate that considers choked flow and non-choked flow conditions based on the upstream P_u to downstream P_d pressure ratio related to the critical value, P_cr, for air.

$$Q = \begin{cases} \frac{C_o A_o C_1 P_u}{\rho\sqrt{T}} & , \frac{P_d}{P_u} \leq 0.528 \\ \frac{C_o A_o C_2 P_u}{\rho\sqrt{T}} (\frac{P_d}{P_u})^{\frac{1}{k}} \sqrt{1-(\frac{P_d}{P_u})^{\frac{1-k}{k}}} & , \frac{P_d}{P_u} > 0.528 \end{cases} \tag{1}$$

Where A_o is the orifice area, C_o is the discharge coefficient, C_1 and C_2 are constants for air, T is the upstream stagnation temperature, ρ is the density, and k is the specific heat ratio.

The orifice meters mentioned earlier are used to approximate the iPAM's power stroke time. Orifice meters were 3D printed using the Original Prusa i3 MK3S+ with a tube diameter of 2.125 mm and orifice radiuses ranging from 2.125 mm (100% open) to 0.425 mm (20% open) (Fig. 7). These orifice meters are fully sealed, meaning no air leakage can occur, hence the orifice area can be directly used in the flow rate equation.

The orifice area has a direct impact on the pressure drop ($P_u - P_d$) that occurs during the iPAM's power stroke. An empirical test was performed using a pressure differential sensor connected to the two ports of the orifice meter, outputting the pressure drop (P_{drop}) across each orifice meter at different supplied pressures ranging from 0 kPa to 300 kPa (Fig. 8a).

A linearly fitted equation was applied to the experimental pressure drop versus supplied pressure data points for each orifice meter pressure drop test. It was found that this linear

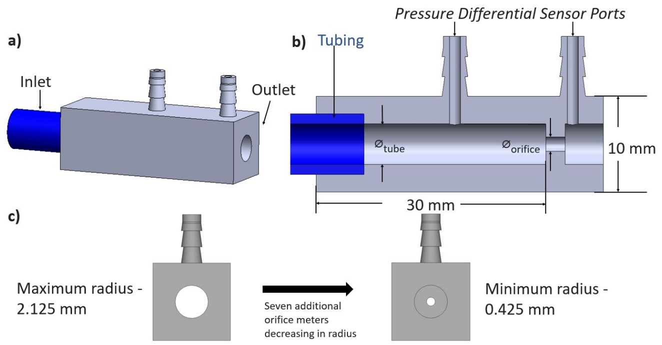

Fig. 7: Custom 3D printed Orifice Meters: ***a)*** A 3D model of the orifice meters used. Eight orifice meters were printed each with different sized orifice radiuses ranging from 0.55 mm to 2.125 mm. ***b)*** A section view shows the tube that is connected to a pressure source that crosses the orifice meter into atmosphere. Pressure differential sensor is connected to the orifice meter ports and measures the difference between the upstream and downstream pressure across the orifice. ***c)*** Outlet port of the orifice showing all the orifice areas tested.

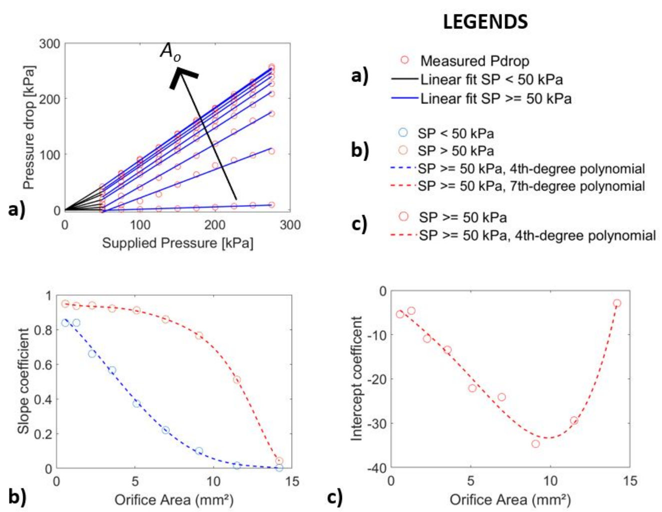

Fig. 8: Orifice Meter Pressure Drop test: ***a)*** Pressure drop versus Supplied pressure plot. Red data points are the measured pressure drop values at a given supplied pressure. Each line indicates a different orifice meter, A_o is orifice area, ranging from the orifice meter that is 100% opened to an orifice meter that is 20% opened. The blue represents the linear function for when $p >= 50$ kPa and the black line is when $p < 50$ kPa. ***b)*** Slope coefficient versus the orifice area and a quadratic fit to the data. Slope coefficient comes from the linearly fitted equations $y = \mathbf{m}x + b$ in sub-figure a. ***c)*** Y-intercept coefficient versus orifice area and a quadratic fit to the data. Y-intercept coefficient comes from the linearly fitted equations $y = mx + \mathbf{b}$ in sub-figure a. The linearly fitted equations for when the supplied pressure is less than 50 kPa has y-intercept coefficient values equal to 0, therefore it is not plotted.

behavior changes when the supplied pressure is less than 50 kPa, requiring the development of a separate linear function for pressure drop as a function of supplied pressure less than 50 kPa (Equation 2). Changing the orifice meter, and thus the orifice area, leads to changes in the slope and y-intercept of the linear equation. To account for this behavior induced by the orifice area, the slope and y-intercepts of the linearly fitted equation for each orifice meter were extracted and used to create additional plots that relate the orifice area to the slope and y-intercept coefficients. Quadratically fitted equations were applied to the slope and y-intercept data sets, Fig. 8b and c respectively. Using these equations, any orifice area can be used to dictate the linear equation of the pressure drop for an orifice meter that is fully sealed given a supplied pressure.

$$P_{\text{drop}}(p) = \begin{cases} m_1(p) + b, & p \geq 50 \text{ kPa} \\ m_2(p), & p < 50 \text{ kPa} \end{cases} \tag{2}$$

Where p is the pressure, m_1 is the slope for when the pressure is greater or equal to 50 kPa, and m_2 is the slope for when the pressure is less than 50 kPa, and b is the y-intercept.

The approximated pressure drop is used with the upstream pressure to determine the downstream pressure, to be used in the flow rate equation. The upstream pressure is assumed to be the pressure coming from the pressure source. Using the approximated pressure drop and upstream pressure the downstream pressure is solved for, $P_{\text{drop}} = P_u - P_d$.

The discharge coefficient is another parameter that needs to be determined to accurately approximate the flow rate. This coefficient is empirically determined and is directly influenced by the orifice area [42]. For the sake of the current discussion, it is assumed that the discharge coefficient is known, but the next section will provide more details on how this coefficient is determined for each orifice meter used. Moving along, the orifice area, downstream pressure, and discharge coefficient are plugged into equation 1, to approximate the flow rate. The orifice area dictates if the flow is treated as choked or non-chocked, since the orifice area directly affects the pressure drop across the orifice, affecting the downstream to upstream pressure ratio. The approximated flow rate and iPAM's change in volume from the previous section, are used to estimate the iPAM's power stroke time using the equation, $Q = \Delta$(Volume)/Time. With the approximated time and iPAM's power stroke displacement from the previous section, the iPAM's contraction displacement versus time curve is approximated, concluding the model.

B. Discharge coefficient approximation

Experimental tests of iPAM contraction rates for different exhaust orifice sizes were first conducted with a 100 g mass attached on the iPAM, with the iPAM being set to a pressure of 250 kPa, Fig 9, for each trial. The solenoid valve is then switched to its closed state engaging the iPAM's power stroke by exhausting its internal pressurized air through the selected orifice meter. This test was performed for all eight 3D printed orifice meters. Slow motion 960fps videos were taken and Kinovea was used for motion capture analysis to obtain the experimental iPAM contraction position over time.

The approach for determining the discharge coefficient from experimentally measured contraction rates involves iterating the model 1000 times with the discharge coefficient varying from 0 to 1.0. During each iteration, the approximated iPAM contraction is compared to the experimental iPAM contraction, and a scoring system is used to evaluate how well the selected discharge coefficient outputs a model that fits the experimental

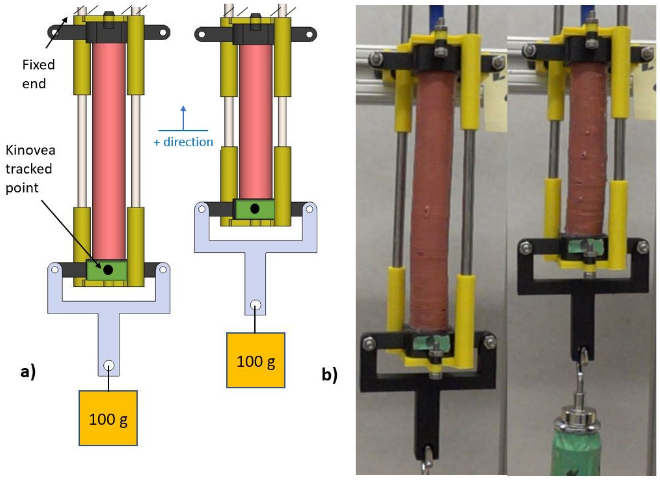

Fig. 9: iPAM contraction test: ***a)*** The iPAM is fixed on one end and the other end is free to move. The iPAM contracts resulting in the free end moving upwards towards the fixed end. ***b)*** Images of the experimental setup are shown, with the iPAM in its inflated (250 kPa supplied) then contracted state, with a 100 g mass hooked on it. Slow-motion videos were captured at 960 fps and Kinovea was used to track the black marker and obtain the iPAM contraction position over time.

data. The score is based on the number of points in the approximated iPAM contraction that fall within the standard deviation region of the experimental data. A higher number of points within the standard deviation region corresponds to a better fit between the model and the experimental data. The discharge coefficients that had the second and third best scores are used to setup the lower and upper bounds for a second iteration of discharge coefficients. This new range is used for a second iteration of 1000 discharge coefficients to further narrow down on a single discharge coefficient with the best score that corresponds to the model that has the best fit to the experimental data (Fig. 10a). This procedure is repeated for each orifice meter, because as stated before the orifice area influences the discharge coefficient. With the best fitted discharge coefficient for all eight orifice meters determined, a function with a polynomial order of 5 was created that takes in an orifice area and outputs the corresponding discharge coefficient (Fig. 10b).

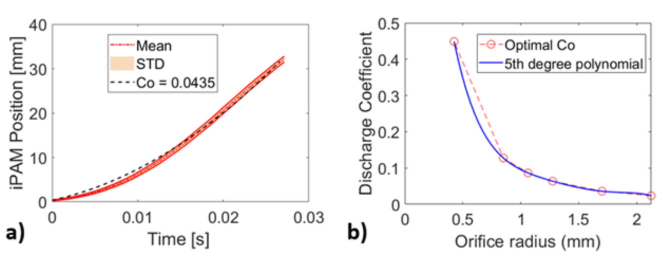

Fig. 10: Discharge Coefficient Approximation Plots: ***a)*** The best scored Co being selected and plotted against the empirical data. ***b)*** Orifice radius (can be easily converted to its area if required), versus discharge coefficient plot with a fitted function to the data. Is used to output a discharge coefficient for a given orifice radius.

C. Relating the SOFD's input to the orifice meters

To obtain an accurate approximation of the SOFD orifice area, an additional pressure drop empirical test is conducted to determine the relationship between the SOFD's input and the pressure drop (Fig. 11a). Measuring the orifice area directly from the rack obstructing the outlet of the SOFD would lead to inaccurate flow rate calculations, as the SOFD is not fully sealed, resulting in an approximation that does not reflect the actual pressure drop across the SOFD. Instead, the slope coefficient is used to establish a relationship between the SOFD's input, and an effective area represented by the orifice meter empirical testing (Fig. 11b). This effective orifice area is used in conjunction with the quintic function derived in Figure. 10b, to obtain a corresponding discharge coefficient value. These two parameters are then incorporated into the model, together with the initial internal pressure of the iPAM, to generate an approximated curve of the iPAM's contraction over time, with the SOFD acting as the flow regulation device.

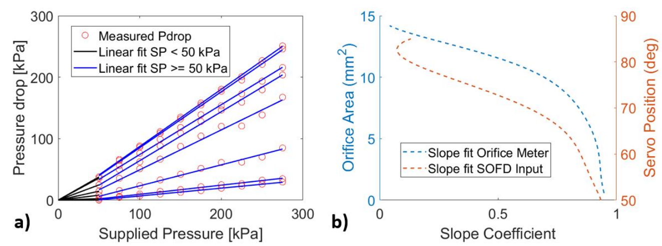

Fig. 11: SOFD Pressure Drop Test: ***a)*** The same pressure drop experiment as for the orifice meters is performed, but with the SOFD. The red points in the graph represent the measured pressure drops at a specific supply pressure for various angular positions of the SOFD. ***b)*** A double y-axis plot is shown, with the slope coefficient on the shared x-axis. This slope coefficient can be used to determine the corresponding effective orifice area given an SOFD input. The two y-axes represent the effective orifice area (in square millimeters) and the angular position of the SOFD (in degrees), respectively.

D. Projectile maximum Launch Height Approximation

The vertical catapult launches a 100g projectile, driven by the iPAM's power stroke, as depicted in Fig. 20. The crucial factor is the iPAM's maximum velocity during contraction. Once the iPAM reaches its maximum velocity, all its energy transfers to the launch plate and thereby the mass. Once launched, there are no further constraints on the projectile. The iPAM's maximum velocity occurs at the beginning of its power stroke when it's at maximum extension and internal air pressure. As the iPAM exhausts its internal air, it gradually slows down. This velocity is obtained by analyzing the model's iPAM contraction displacement over time output. This output is differentiated to obtain the iPAM's velocity during its power stroke and therefore the maximum velocity can be determined. The initial height of the plate is considered, as this is when the mass's energy is entirely kinetic, due to the maximum velocity of the iPAM occurring at the beginning of the power stroke. Upon reaching maximum height, the energy transforms into potential energy. Applying the conservation of energy, the total displacement of the projectile can be determined. However, we are specifically interested in the projectile's launch height which is the distance traveled in the air while not in contact with the launch plate. Equation 3 accounts for this and enables the calculation of the launch height for a 100g mass.

$$h_{projectile} = \frac{v_{max}^2}{2g} - (plate_{final} - plate_{initial}) \qquad (3)$$

Where $h_{projectile}$ is the projectile's launch height, v_{max} is the maximum velocity of the iPAM during its power stroke, g is gravity, $plate_{final}$ is the launch plate's final position during the iPAM's power stroke, and $plate_{intial}$ is the launch plate's initial position during the iPAM's power stroke.

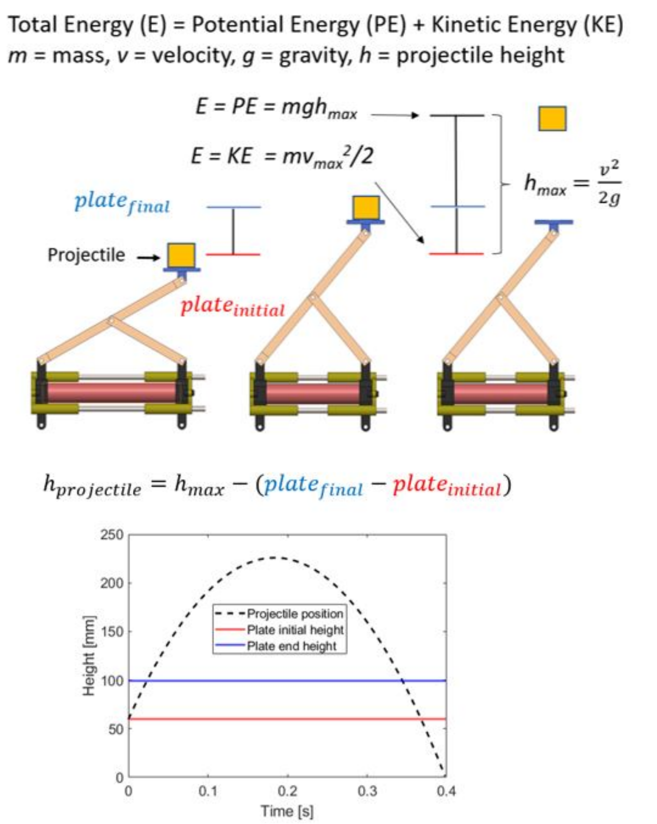

Fig. 12: Vertical Catapult Launching Motion: The proposed vertical catapult is designed to launch a 100 g projectile. The iPAM is what drives the vertical catapult, and its maximum velocity dictates the launch height the projectile will reach. Using the model the maximum velocity of the iPAM is obtained. Using this velocity, the launch plate's initial and final position throughout the launch, along with the principles of the conservation of energy the projectile's launch height can be calculated.

IV. Results

A. Experimental and predicted analysis of iPAM contraction using the SOFD as an exhaust air flow regulator

The SOFD was used as the exhaust air flow regulator on the same experimental setup as in Fig. 9, with the iPAM having an initial internal pressure of 250 kPa and a 100 g weight attached to it. Slow-motion videos of the iPAM contracting at six different SOFD inputs, ranging from 0 % open to 100% open, were captured. The videos were recorded at 960 fps, and the iPAM's contraction displacement versus time data was collected through Kinovea, a motion capture software. Approximated iPAM contraction displacement versus time data was generated following the workflow from Section C in the Methodology section. The inputs used for the experimental data were repeated for the modeled data, generating five approximated iPAM contraction versus time data, ranging from 0 % to 100 % open. Fig. 13, shows the iPAM's contraction displacement experimental data along with the modeled version.

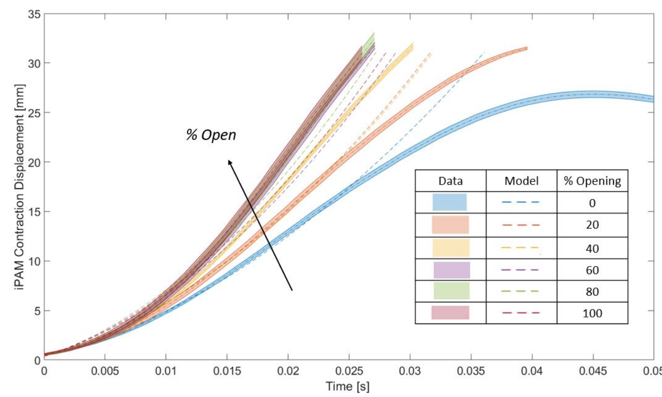

Fig. 13: iPAM contraction displacement versus time: A iPAM contraction displacement versus time plot comparing the experimental data with approximated data. Each shaded region represents the experimental data, the dashed curves represent the model's output, and each colour represents a different SOFD input in terms of percentage opened.

B. Testing the iPAM contraction model to predict projectile maximum launch height using a vertical catapult

The vertical catapult was used to test out the workflow strategy described in Section D of the Methodology section, to test if the iPAM contraction versus time model can be used to predict the projectile's maximum launch height. The same conditions were used as for the iPAM contraction experiments, with the iPAM's initial internal pressure being set to 250 kPa and launching a 100 g mass at the six SOFD inputs, ranging from 0 % to 100 % open. Using Kinovea, the maximum projectile height of each launch was recorded. Using these same SOFD inputs the iPAM contraction model as described in Section C of the workflow diagram was generated, then Section D was followed to come up with predicted projectile launch height values for each SOFD input. Fig. 14, shows how the predicted heights compare with the experimental heights. Additionally, Table I represents the percentage error between the mean experimental launch height against the predicted launch height for all SOFD inputs tested.

V. Discussion & Future Work

The successful modulation of the iPAM's power by the SOFD is illustrated in Fig. 13. As the SOFD's % opening increased, the time for the iPAM's power stroke decreased, indicating an increase in the power of the iPAM. This relationship is consistent with the equation for power (Power = Work/time), where time is inversely proportional to power.

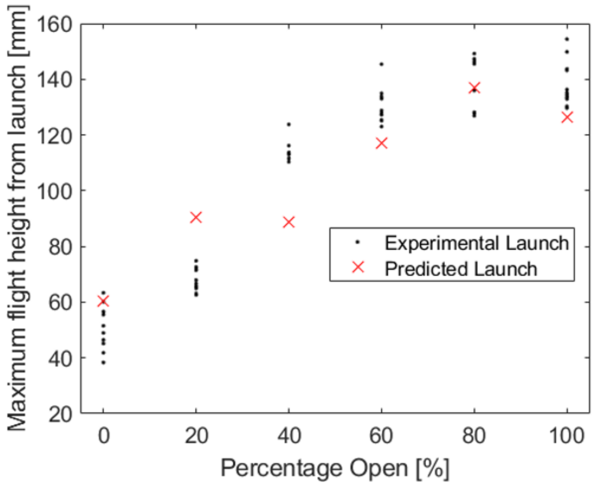

Fig. 14: Vertical Catapult Projectile Launching Experimental vs Predicted: Results of the launch testing representing the maximum flight height of the projectile with the corresponding SOFD input. The SOFD input is represented by the percentage of the orifice area to tube diameter ratio. The black dots represent experimental launches, and the red circle represents predicted launch height.

TABLE I: Experimentally measured launch heights compared with model predictions for different SOFD regulator settings.

% open	Experimental launch height [mm]	Model launch height [mm]	% error
0	50.395 ± 7.790	60.400	16.565*
20	68.145 ± 4.252	90.494	24.697
40	114.150 ± 3.978	88.868	-28.449**
60	130.702 ± 6.312	117.246	-11.476
80	138.415 ± 9.727	136.846	-1.416
100	138.452 ± 8.169	126.438	-9.502

* Positive percentage error corresponds to a predicted launch height that is greater than the experimental mean launch height.

** Negative percentage error corresponds to a predicted launch height that is less than the experimental mean launch height.

The flow rate and orifice area are directly proportional, as seen in the flow rate equation (Equation 1), and the flow rate affects the time. The proposed methodology enabled the model to follow the trend of the experimental data and capture the effects of the changing SOFD input. The results of the vertical catapult test in Fig. 14, also reflect the iPAM's power modulation by having different projectile's maximum launch heights at different SOFD inputs. As with the iPAM contraction, it was expected that the projectile's maximum launch height increased with the SOFD's % opening increasing because the iPAM's contraction rate increases with an increase to SOFD % opening.

Looking at Table I at the lower SOFD % openings it is evident that the model's predicted launch heights are overshooting, estimating higher launch heights than what was experimentally observed. This is because the model doesn't consider the iPAM interacting with an opposing force that occurs from the damping effect at lower SOFD % openings. During the iPAM's contraction, it reaches a point where a terminal exhaust flow speed is reached before the iPAM's internal air is fully exhausted. The iPAM's latex tubing picks up speed as it contracts, however it encounters the compressed air that has been built up internally and can not exceed that terminal exhaust flow speed. Due to the iPAM being made from soft materials it behaves like a spring and rebounds against that compressed air inside and stretches back. That initial rapid displacement of the iPAM is of interest since this is what contributes to the work done by the iPAM and the energy transferred to the projectile being launched. The model assumes that the iPAM's contracts to its original position without any disturbances and that it stops at the displacement that was measured when 250 kPa is applied to the iPAM, determined from the pressure versus displacement characterization in Fig. 6. Considering this, it becomes apparent that the model tends to overshoot because it predicts the iPAM's displacement to be greater within the same time frame compared to the actual iPAM displacement, which is less. Fig. 23 illustrates the comparison between the actual iPAM's contraction displacement with a SOFD % opening of 0 % and the model's estimated iPAM contraction.

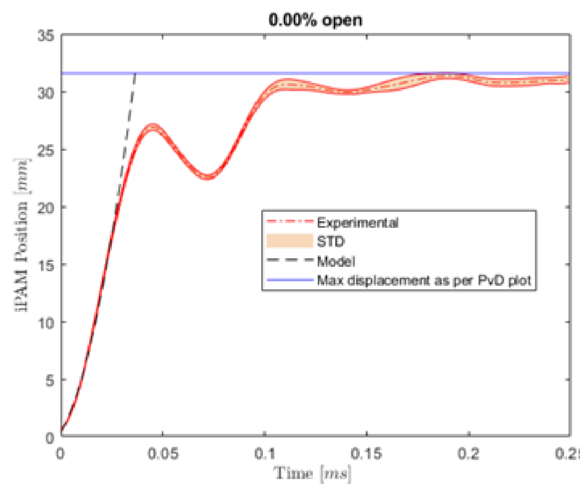

Fig. 15: Air spring damping effect incurred at lower SOFD % openings: iPAM displacement versus time plot during the iPAM's contraction with the SOFD being set to 0 % opening. It is evident that that the model is overshooting the power outputted by the iPAM because it reaches the iPAM's original position much quicker than the actual iPAM at this SOFD input.

Once again, referring to Table I, it is evident that at higher SOFD % openings, the model's predicted launch heights fall short compared to the actual launches. Fig. 16 illustrates the iPAM's contraction displacement with the SOFD % opening set at 100 %. At higher SOFD % openings, the iPAM's initial contraction exceeds the maximum displacement as per the pressure versus displacement characterization shown in Fig. 6. In this scenario, the iPAM exhausts its internal air without any obstruction, and due to the soft material properties of the latex tubing, it carries its momentum forward, bending in on itself, resulting in further displacement than anticipated (Fig. 16b). The extra displacement obtained from the iPAM stretching contributes to increased work done by the iPAM, generating more power. As mentioned earlier, the model does not account for the possibility of the iPAM displacing beyond its original length, leading to a reduced power output in comparison to reality, where more work is actually done by the iPAM.

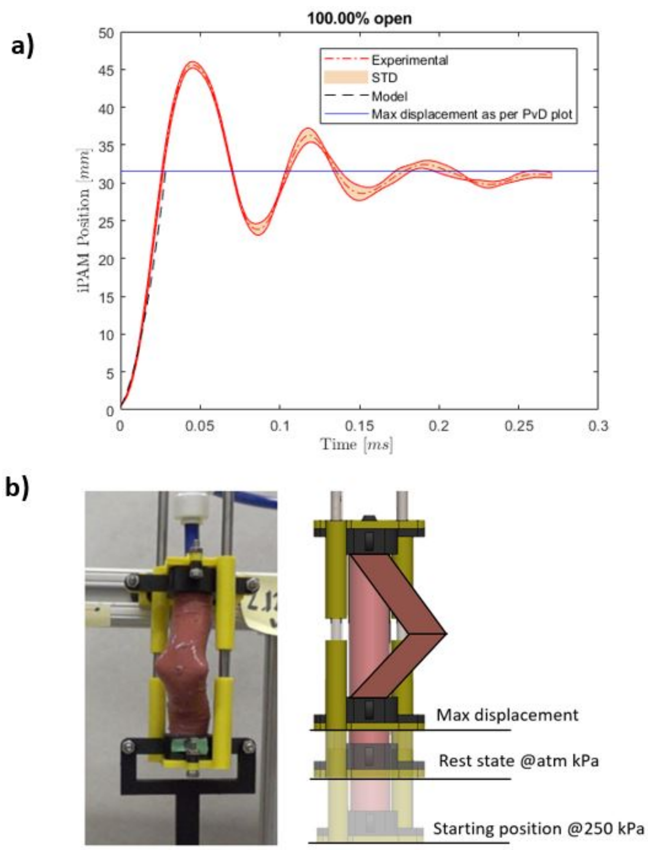

Fig. 16: Contraction displacement exceeding iPAM's original length at greater SOFD % openings: ***a)*** iPAM contraction displacement plot at a SOFD input set to 100 % open showing demonstrating the difference in displacement between the model and what was observed. ***b)*** A screenshot of the moment when the iPAM bends in on itself, along with an illustration highlighting the effect more clearly.

At a SOFD input set to 40 % open, the model's estimated launch height undershoots by 28.45 % compared to the mean of the observed launch heights at that SOFD input. This highlights the sensitivity issues of the model. Following Fig. 11b, a servo degree of 64, which translates to 40 %, results in an orifice area of 8.5135 mm2, which corresponds to a 1.6462 mm orifice radius. Fig. 17a is the same Co versus orifice radius plot as in Fig. 10b, but focuses on the two points where the corresponding orifice radius of 1.6462 mm falls between. Fig. 17b, has a plot showing the model's iPAM contraction displacement fixed at an orifice radius of 1.6462 mm, iterating through five different Co values that the selected orifice radius range corresponds to. Visually it can be seen that there is variability between each modeled output, highlighting the effect the Co value has on the model's iPAM contraction displacement output.

In Fig. 14, the variability in experimental launches comes from various factors such as friction between all the moving components, the level of the launch plate when launching, the behavior of the iPAM between each launch, and the rack of the SOFD. After each launch the exhaust air coming from the iPAM can potentially change the linear position of the

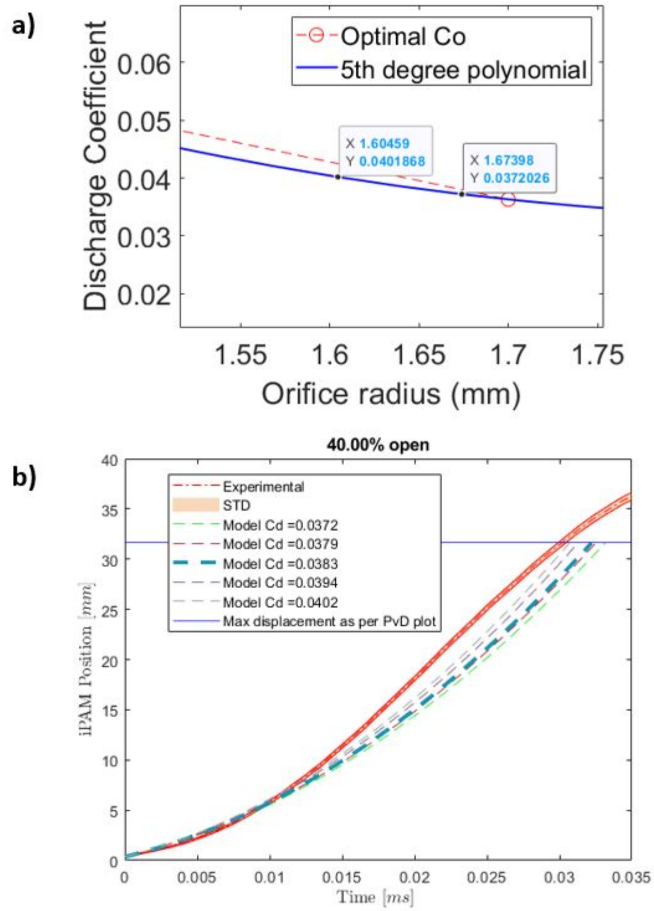

Fig. 17: Detailed look at the effect the Co value has on model's output at an SOFD input set to 40 % opened ***a)*** Same discharge coefficient versus orifice radius plot as in Fig. 18b, but zoomed in on two points where a 40 % SOFD input falls between. ***b)*** The model is iterated through five Co values that correspond to the selected orifice radius range, with a fixed orifice radius of 1.6462 mm (corresponds to 40 % SOFD input) to see the effects the Co value has on the model's output.

SOFD rack changing the % opening. Due to the area being worked with here being at most 16 mm2, a slight change in the linear position can have a large impact. Another source of error comes from the iPAM stretching further when the mass is placed on the launch plate. With the end cap not being support in the vertical catapult mechanism, when the iPAM is inflated and extended the moment arm is increased. Consequently, when the mass is placed it pushes the launch plate further down, extending the iPAM further. The model does not account for this extra extension incurred by the mass, which results in an increased displacement of the iPAM's contraction. With all these potential sources of error for the repeatability of the vertical catapult, at most the variability between each launch with the same SOFD input is approximately ± 10 mm. Considering that its possible to launch the projectile from around 50 mm high to 140 mm high, the variability does not get in the way of observing the effects different SOFD inputs have on the launch height.

The purpose of the vertical catapult system was to demonstrate how the iPAM's power can be transferred into a system and given an application, in this case launching a projectile. This system was used because it can be easily adapted to a legged system used for jumping passed obstacles. If you simply invert the proposed mechanism, the launch plate can be used as the 'foot,' something that is in contact with the ground, and the iPAM is now a muscle that when contracting generates the power for the plate to push off the ground and launch the legged system into the air (Previous chapter demonstrates this legged system). Fully implementing this into a mobile legged robot that can jump over obstacles would require a microcontroller to control the SOFD to enable the legged system to jump the correct height over an obstacle. This is where the proposed model comes into play because it makes it possible to create a jump height versus SOFD input curve that can be directly fed into a microcontroller. With this and some sensors mounted on the legged robot, communicating back to the microcontroller the height of an obstacle, the SOFD can be controlled accordingly, inherently setting the desired iPAM's contraction rate leading to a desired jump height. In this work the predicted launch heights can be easily translated to predicted jump heights for a 100 g robot, because the same principles are in effect when launching a mass and when having an object with a certain mass jump. With the predicted jump heights for every SOFD input a characteristic curve can be made and implemented to a 100 g legged jumping system.

VI. Conclusion

The work shown here demonstrates that exhaust flow regulation for a soft pneumatic actuator is an effective method to modulate the mechanical power output of an iPAM, and more generally as a strategy for achieving controllable high-power actuation using SPA driven robotic systems. Moreover, it is shown that exhaust flow regulation can be achieved through the use of a custom proportional valve (SOFD) that is inexpensive, lightweight, and easily fabricated, which is amenable to scaling and customized mobile robot design. The one-time characterization procedure presented along with a flow rate model is shown to be an effective method for predicting actuator performance of controlled power modulation, despite the imperfect, low-tolerance fabrication and construction of the low-cost regulator valve. A vertical catapult mechanism was constructed to validate the efficacy of the flow rate and power modulation model, through comparison of the predicted and measured height of a launched projectile mass. This test system also embodies the morphology and basic function of a robotic limb which could be leveraged in future work as the foundation for a high-power, dynamic legged mobile robotic platform.

VII. Acknowledgement

This work was funded by the Natural Sciences and Engineering Research Council and Queen's Ingenuity Labs Research Institute.

References

[1] A. V. Birn-Jeffery and M. A. Daley, "Birds achieve high robustness in uneven terrain through active control of landing conditions," *Journal of Experimental Biology*, vol. 215, no. 12, pp. 2117–2127, Jun. 2012. [Online]. Available: https://doi.org/10.1242/jeb.065557

[2] J. C. Spagna, D. I. Goldman, P.-C. Lin, D. E. Koditschek, and R. J. Full, "Distributed mechanical feedback in arthropods and robots simplifies control of rapid running on challenging terrain," *Bioinspiration & Biomimetics*, vol. 2, no. 1, p. 9, Jan. 2007. [Online]. Available: https://dx.doi.org/10.1088/1748-3182/2/1/002

[3] A. A. Biewener, R. J. Bomphrey, M. A. Daley, and A. J. Ijspeert, "Stability and manoeuvrability in animal movement: lessons from biology, modelling and robotics," *Proceedings of the Royal Society B: Biological Sciences*, vol. 289, no. 1967, p. 20212492, Jan. 2022, publisher: Royal Society. [Online]. Available: https://royalsocietypublishing.org/doi/full/10.1098/rspb.2021.2492

[4] R. J. Full and D. E. Koditschek, "Templates and anchors: neuromechanical hypotheses of legged locomotion on land," *Journal of Experimental Biology*, vol. 202, no. 23, pp. 3325–3332, Dec. 1999. [Online]. Available: https://doi.org/10.1242/jeb.202.23.3325

[5] A. Torres-Pardo, D. Pinto-Fernández, M. Garabini, F. Angelini, D. Rodriguez-Cianca, S. Massardi, J. Tornero, J. C. Moreno, and D. Torricelli, "Legged locomotion over irregular terrains: state of the art of human and robot performance," *Bioinspiration & Biomimetics*, vol. 17, no. 6, p. 061002, Oct. 2022, publisher: IOP Publishing. [Online]. Available: https://dx.doi.org/10.1088/1748-3190/ac92b3

[6] "Metal or muscle? The future of biologically inspired robots | Science Robotics." [Online]. Available: https://www.science.org/doi/full/10.1126/scirobotics.aba6149?casa_token=ZzkT8fSb7swAAAAA:twKLsazKBFWnR2RNT4AfFoWs3pRrEo3IX7f5oeZCFYRuXXHKj4e7q9mOg8iiWVvIbqTGnLroLc_mvA

[7] F. Ahmed, M. Waqas, B. Jawed, A. M. Soomro, S. Kumar, A. Hina, U. Khan, K. H. Kim, and K. H. Choi, "Decade of bio-inspired soft robots: a review," *Smart Materials and Structures*, vol. 31, no. 7, p. 073002, Jun. 2022, publisher: IOP Publishing. [Online]. Available: https://dx.doi.org/10.1088/1361-665X/ac6e15

[8] X. Mo, W. Ge, M. Miraglia, F. Inglese, D. Zhao, C. Stefanini, and D. Romano, "Jumping Locomotion Strategies: From Animals to Bioinspired Robots," *Applied Sciences*, vol. 10, no. 23, p. 8607, Jan. 2020, number: 23 Publisher: Multidisciplinary Digital Publishing Institute. [Online]. Available: https://www.mdpi.com/2076-3417/10/23/8607

[9] G. Picardi, A. Astolfi, D. Chatzievangelou, J. Aguzzi, and M. Calisti, "Underwater legged robotics: review and perspectives," *Bioinspiration & Biomimetics*, vol. 18, no. 3, p. 031001, Apr. 2023, publisher: IOP Publishing. [Online]. Available: https://dx.doi.org/10.1088/1748-3190/acc0bb

[10] S. Saeedvand, M. Jafari, H. S. Aghdasi, and J. Baltes, "A comprehensive survey on humanoid robot development," *The Knowledge Engineering Review*, vol. 34, p. e20, Jan. 2019, publisher: Cambridge University Press. [Online]. Available: https://www.cambridge.org/core/journals/knowledge-engineering-review/article/comprehensive-survey-on-humanoid-robot-development/CC2428375A1F38DD94079125FD8A45B6

[11] C. Hubicki, J. Grimes, M. Jones, D. Renjewski, A. Spröwitz, A. Abate, and J. Hurst, "ATRIAS: Design and validation of a tether-free 3D-capable spring-mass bipedal robot," *The International Journal of Robotics Research*, vol. 35, no. 12, pp. 1497–1521, Oct. 2016. [Online]. Available: http://journals.sagepub.com/doi/10.1177/0278364916648388

[12] J. Hurst, "Walk this way: To be useful around people, robots need to learn how to move like we do," *IEEE Spectrum*, vol. 56, no. 3, pp. 30–51, Mar. 2019, conference Name: IEEE Spectrum.

[13] E. Guizzo, "By leaps and bounds: An exclusive look at how Boston dynamics is redefining robot agility," *IEEE Spectrum*, vol. 56, no. 12, pp. 34–39, Dec. 2019, conference Name: IEEE Spectrum.

[14] M. Hutter, C. Gehring, A. Lauber, F. Gunther, C. D. Bellicoso, V. Tsounis, P. Fankhauser, R. Diethelm, S. Bachmann, M. Bloesch, H. Kolvenbach, M. Bjelonic, L. Isler, and K. Meyer, "ANYmal - toward legged robots for harsh environments," *Advanced Robotics*, vol. 31, no. 17, pp. 918–931, Sep. 2017, publisher: Taylor & Francis _eprint: https://doi.org/10.1080/01691864.2017.1378591. [Online]. Available: https://doi.org/10.1080/01691864.2017.1378591

[15] S. Seok, A. Wang, M. Y. Chuah, D. Otten, J. Lang, and S. Kim, "Design principles for highly efficient quadrupeds and implementation on the MIT Cheetah robot," in *2013 IEEE International Conference on Robotics and Automation*, May 2013, pp. 3307–3312, iSSN: 1050-4729.

[16] G. Kenneally, A. De, and D. E. Koditschek, "Design Principles for a Family of Direct-Drive Legged Robots," *IEEE Robotics and Automation Letters*, vol. 1, no. 2, pp. 900–907, Jul. 2016, conference Name: IEEE Robotics and Automation Letters.

[17] G. Pratt and M. Williamson, "Series elastic actuators," in *Proceedings 1995 IEEE/RSJ International Conference on Intelligent Robots and*

Systems. Human Robot Interaction and Cooperative Robots, vol. 1, Aug. 1995, pp. 399–406 vol.1.

[18] G. P. Sutton, E. Mendoza, E. Azizi, S. J. Longo, J. P. Olberding, M. Ilton, and S. N. Patek, "Why do Large Animals Never Actuate Their Jumps with Latch-Mediated Springs? Because They can Jump Higher Without Them," *Integrative and Comparative Biology*, vol. 59, no. 6, pp. 1609–1618, Dec. 2019. [Online]. Available: https://doi.org/10.1093/icb/icz145

[19] V. Klemm, A. Morra, C. Salzmann, F. Tschopp, K. Bodie, L. Gulich, N. Küng, D. Mannhart, C. Pfister, M. Vierneisel, F. Weber, R. Deuber, and R. Siegwart, "Ascento: A Two-Wheeled Jumping Robot," in *2019 International Conference on Robotics and Automation (ICRA)*, May 2019, pp. 7515–7521, iSSN: 2577-087X.

[20] "Boston Dynamics Sand Flea Robot Demonstrates Astonishing Jumping Skills - IEEE Spectrum." [Online]. Available: https://spectrum.ieee.org/boston-dynamics-sand-flea-demonstrates-astonishing-jumping-skills

[21] D. W. Haldane, J. K. Yim, and R. S. Fearing, "Repetitive extreme-acceleration (14-g) spatial jumping with Salto-1P," in *2017 IEEE/RSJ International Conference on Intelligent Robots and Systems (IROS)*, Sep. 2017, pp. 3345–3351, iSSN: 2153-0866.

[22] M. Kovac, M. Fuchs, A. Guignard, J.-C. Zufferey, and D. Floreano, "A miniature 7g jumping robot," in *2008 IEEE International Conference on Robotics and Automation*, May 2008, pp. 373–378, iSSN: 1050-4729.

[23] V. Zaitsev, O. Gvirsman, U. B. Hanan, A. Weiss, A. Ayali, and G. Kosa, "A locust-inspired miniature jumping robot," *Bioinspiration & Biomimetics*, vol. 10, no. 6, p. 066012, Nov. 2015, publisher: IOP Publishing. [Online]. Available: https://dx.doi.org/10.1088/1748-3190/10/6/066012

[24] L. Tang, X. Wu, P. Liu, Y. Li, and B. Li, "The Feedback Trajectory Control of a SMA-Driven Miniature Jumping Robot," in *2022 International Conference on Robotics and Automation (ICRA)*, May 2022, pp. 9769–9775.

[25] X. Bai, D. Kong, Q. Wang, X. Yu, and X. Xie, "Bionic Design of a Miniature Jumping Robot," *Applied Sciences*, vol. 13, no. 7, p. 4534, Jan. 2023, number: 7 Publisher: Multidisciplinary Digital Publishing Institute. [Online]. Available: https://www.mdpi.com/2076-3417/13/7/4534

[26] B. Kalita, A. Leonessa, and S. K. Dwivedy, "A Review on the Development of Pneumatic Artificial Muscle Actuators: Force Model and Application," *Actuators*, vol. 11, no. 10, p. 288, Oct. 2022, number: 10 Publisher: Multidisciplinary Digital Publishing Institute. [Online]. Available: https://www.mdpi.com/2076-0825/11/10/288

[27] C.-P. Chou and B. Hannaford, "Measurement and modeling of McKibben pneumatic artificial muscles," *IEEE Transactions on Robotics and Automation*, vol. 12, no. 1, pp. 90–102, Feb. 1996, conference Name: IEEE Transactions on Robotics and Automation.

[28] "Soft Robotics: Review of Fluid-Driven Intrinsically Soft Devices; Manufacturing, Sensing, Control, and Applications in Human-Robot Interaction - Polygerinos - 2017 - Advanced Engineering Materials - Wiley Online Library." [Online]. Available: https://onlinelibrary.wiley.com/doi/abs/10.1002/adem.201700016?casa_token=iA5_TSYJJZ0AAAAA:OIebCDC7mDBPkF0wM8UhBGfvg13VSD9Qbn7gkthne_tl2uHGTiwTsZOA7vG03CD37f7yNKSM05SGbjc

[29] C. Majidi, "Soft Robotics: A Perspective—Current Trends and Prospects for the Future," *Soft Robotics*, vol. 1, no. 1, pp. 5–11, Mar. 2014, publisher: Mary Ann Liebert, Inc., publishers. [Online]. Available: https://www.liebertpub.com/doi/abs/10.1089/soro.2013.0001

[30] R. Niiyama, A. Nagakubo, and Y. Kuniyoshi, "Mowgli: A Bipedal Jumping and Landing Robot with an Artificial Musculoskeletal System," in *Proceedings 2007 IEEE International Conference on Robotics and Automation*, Apr. 2007, pp. 2546–2551, iSSN: 1050-4729.

[31] K. Luo, P. Rothemund, G. M. Whitesides, and Z. Suo, "Soft kink valves," *Journal of the Mechanics and Physics of Solids*, vol. 131, pp. 230–239, Oct. 2019. [Online]. Available: https://www.sciencedirect.com/science/article/pii/S0022509619303473

[32] R. Balak and Y. C. Mazumdar, "Bistable Valves for MR Fluid-Based Soft Robotic Actuation Systems," *IEEE Robotics and Automation Letters*, vol. 6, no. 4, pp. 8285–8292, Oct. 2021, conference Name: IEEE Robotics and Automation Letters.

[33] S. Wang, L. He, and P. Maiolino, "Design and Characterization of a 3D-Printed Pneumatically-Driven Bistable Valve With Tunable Characteristics," *IEEE Robotics and Automation Letters*, vol. 7, no. 1, pp. 112–119, Jan. 2022, conference Name: IEEE Robotics and Automation Letters.

[34] C. J. Decker, H. J. Jiang, M. P. Nemitz, S. E. Root, A. Rajappan, J. T. Alvarez, J. Tracz, L. Wille, D. J. Preston, and G. M. Whitesides, "Programmable soft valves for digital and analog control," *Proceedings of the National Academy of Sciences*, vol. 119, no. 40, p. e2205922119, Oct. 2022, publisher: Proceedings of the National Academy of Sciences. [Online]. Available: https://www.pnas.org/doi/abs/10.1073/pnas.2205922119

[35] R. S. Diteesawat, T. Helps, M. Taghavi, and J. Rossiter, "Electro-pneumatic pumps for soft robotics," *Science Robotics*, vol. 6, no. 51, p. eabc3721, Feb. 2021, publisher: American Association for the Advancement of Science. [Online]. Available: https://www.science.org/doi/full/10.1126/scirobotics.abc3721

[36] W. Tang, C. Zhang, Y. Zhong, P. Zhu, Y. Hu, Z. Jiao, X. Wei, G. Lu, J. Wang, Y. Liang, Y. Lin, W. Wang, H. Yang, and J. Zou, "Customizing a self-healing soft pump for robot," *Nature Communications*, vol. 12, no. 1, p. 2247, Apr. 2021, number: 1 Publisher: Nature Publishing Group. [Online]. Available: https://www.nature.com/articles/s41467-021-22391-x

[37] D. Drotman, S. Jadhav, D. Sharp, C. Chan, and M. T. Tolley, "Electronics-free pneumatic circuits for controlling soft-legged robots," *Science Robotics*, vol. 6, no. 51, p. eaay2627, 2021. [Online]. Available: https://www.science.org/doi/abs/10.1126/scirobotics.aay2627

[38] M. Garrad, G. Soter, A. T. Conn, H. Hauser, and J. Rossiter, "A soft matter computer for soft robots," *Science Robotics*, vol. 4, no. 33, p. eaaw6060, Aug. 2019, publisher: American Association for the Advancement of Science. [Online]. Available: https://www.science.org/doi/10.1126/scirobotics.aaw6060

[39] S. T. Mahon, A. Buchoux, M. E. Sayed, L. Teng, and A. A. Stokes, "Soft Robots for Extreme Environments: Removing Electronic Control," in *2019 2nd IEEE International Conference on Soft Robotics (RoboSoft)*, Apr. 2019, pp. 782–787.

[40] E. W. Hawkes, D. L. Christensen, and A. M. Okamura, "Design and implementation of a 300% strain soft artificial muscle," in *2016 IEEE International Conference on Robotics and Automation (ICRA)*, May 2016, pp. 4022–4029.

[41] E. Richer and Y. Hurmuzlu, "A High Performance Pneumatic Force Actuator System: Part I—Nonlinear Mathematical Model," *Journal of Dynamic Systems, Measurement, and Control*, vol. 122, no. 3, pp. 416–425, Jun. 1999. [Online]. Available: https://doi.org/10.1115/1.1286336

[42] B. R. Munson, T. H. Okiishi, W. W. Huebsch, and A. P. Rothmayer, *Fundamentals of Fluid Mechanics*, 7th ed. John Wiley & Sons, Inc, 1990.